Multiple-scattering effects for the propagation of light in 3D slabs

1990 J. Phys.: Condens. Matter 2 7653

(http://iopscience.iop.org/0953-8984/2/37/010)

J. Phys.: Condens. Matter 2 (1990) 7653–7677. Printed in the UK

Multiple-scattering effects for the propagation of light in 3D slabs

B A van Tiggelen†, A Lagendijk†‡ and A Tip†

† FOM-Institute for Atomic and Molecular Physics, Kruislaan 407, 1098 SJ Amsterdam, The Netherlands

‡ Natuurkundig Laboratorium, Universiteit van Amsterdam, Valckenierstraat 65, 1018 XE Amsterdam, The Netherlands

Received 13 March 1990

Abstract. A consistent theory for coherent multiple isotropic scalar and Rayleigh vector scattering is presented using a point interaction model for the scatterers. A diagrammatic expansion is employed and new interesting coherent effects are discussed. Dependent-scattering corrections are calculated for the dielectric constant and the scattering mean free path. Intensity diagrams are considered and, in particular, the contribution of closed light paths (loops) is investigated. A new coherent feature is identified: a forward cone but, because of its density dependence, it will be difficult to detect this cone experimentally.

1. Introduction

Interference phenomena in light propagation have been given much attention lately. It has been realised that light paths that are time-reversed with respect to the usual incoherent contribution [1] give rise to enhanced backscattering. As every incoherent scattering event, except for the single-scattering contribution, has a time-reversed variant, an enhancement factor slightly less than two is expected. This has been verified experimentally, although there were indications that this factor is less than expected on the basis of single-scattering events alone [2] . Diagrammatic theories for both isotropic scalar [2, 3] and Rayleigh vector scatterers [4, 5] were set up and were found to agree quite well with experiments. Recently three new polarisation effects in coherent backscattering were reported [6, 7] and explained on the basis of low-order scattering events for which polarisation effects are not averaged out.

In diagrammatic theory, the enhanced backscattering, also known as *weak localisation*, is described by the 'most-crossed' diagrams which predict a cone in the backscattered light with typical angular width $\Delta\theta \approx (k\bar{l}_{\rm tr})^{-1}$, where $\bar{l}_{\rm tr}$ is the transport mean free path and k is the wavenumber in the medium. The vanishing of diffusion, known as *strong localisation*, is associated with these diagrams as well. This idea has been worked out analytically for electron waves [8] and, later, also for acoustic waves [9] on the basis of perturbation theory. This theory is expected to apply when the scattering mean free path $\bar{l}$ is much larger than the wavelength in the medium: $k\bar{l} \gg 1$. The onset of strong localisation in three dimensions is often assumed to be satisfied simultaneously with the *Ioffe–Regel criterion*

$$k\bar{l}_{\rm tr} = 1. \tag{1.1}$$

0953-8984/90/377653+25$03.50

It should be emphasised that $\bar{l}_{tr}$ is a fundamental transport property, directly related to diffusion, whereas the scattering mean free path $\bar{l}$ is a length scale of the amplitude Green function. Therefore, a study of the scattering mean free path cannot give information about the location of the mobility edge, although equation (1.1) is sometimes replaced by the condition $k\bar{l} = 1$ simply because the quantity $k\bar{l}$ is much easier to calculate. The major problem with this condition [10] is that it seems to predict a mobility edge independent of the dimensionality of the system, which is in contradiction to scaling theories. In principle, both $\bar{l}$ and $\bar{l}_{tr}$ are accessible via transmission experiments. In the lowest order of the density, perturbation theory predicts them to be related according to the Boltzmann formula

$$\bar{l}_{tr} = \frac{\bar{l}}{1 - \langle \cos\theta \rangle} \tag{1.2}$$

where $\langle \cos\theta \rangle$ is the average cosine of the scattering angle. For an isotropic or Rayleigh phase function this quantity is equal to zero.

The article is organised as follows: in section 2 we will give a definition of our point interactions, without going into much detail. In section 3 the averaged amplitude Green function is evaluated both for scalar isotropic and Rayleigh vector point scatterers. It is then possible to give the effective dielectric constant and the scattering mean free path as functions of the density of the scattering particles. Section 4 deals with contributions to the scattered intensity coming from diagrams involving two Rayleigh vector scatterers. In section 5 recurrent light paths (loops) with more scatterers are discussed. Because of their complex nature, we restricted ourselves to a scalar approach. Loops are important for two reasons. Firstly they are equal to their time-reversed variant and, thus, present a special case among the subset of diagrams that do have a time-reversed equivalent. They give a positive angle-independent contribution to the scattered intensity and will therefore reduce, in principle, the enhanced backscattering factor below two. Secondly, the loops turn out to have a coherent equivalent as well, though not at backscattering: their coherent variants, to which we shall refer as *forward-crossed*, give constructive interference behind the slab. The angular dependence and their density dependence will be discussed.

2. Point scatterers

Generally speaking scattering calculations are greatly simplified if the interaction causing the scattering phenomenon is separable. On the other hand, physical potentials are local, i.e. functions of position only. If one insists on having both features simultaneously one is led to point interactions such as the δ-potential in one, and the Fermi potential in three dimensions (for a thorough study of such point interactions see [11]). A point interaction can also be interpreted as a boundary condition imposed on the domain of the non-perturbed generator of the time evolution (the Hamiltonian—Δ in the Schrödinger situation). In the Schrödinger case in more than three dimensions, as well as in the Maxwell case, this strategy breaks down: it is impossible to obtain a self-adjoint time evolution generator, which is different from the non-perturbed one in this way (in mathematical terms: we encounter a case of essential self-adjointness). Nevertheless, Grossmann and Wu [12] and Wu [13] found objects which have many properties of the resolvent (Green function) for the Schrödinger case in five dimensions and the Maxwell case, respectively. In fact both cases turned out to be quite

analogous mathematically. In particular, scattering quantities could be calculated. A property that was lacking was a square integrability property, so that Hilbert space vectors were mapped out of the space.

It was suggested by these authors that the problem could be given a rigorous basis using a Pontrjagin space formalism. This was taken up by van Diejen and Tip [14] who found that such an approach indeed works and that scattering quantities can be rigorously defined as objects in the original Hilbert space using a 'two Hilbert space' set-up. The resulting scattering operator is unitary and the optical theorem holds. There is also a canonical way to obtain the relevant point interaction. In the case of electromagnetic scattering from a dielectric sphere (Mie scattering), one obtains a corresponding unique point-interaction model having the same asymptotical behaviour at low energies. An arbitrary number N of point scatterers can be accommodated in this way while retaining the important property valid for N separable interactions in the conventional situation: the calculation of the N-scatterer T-matrix merely requires the handling of a complex $N \times N$ matrix. For scalar scattering the situation is similar. In that case the vector wave equation is replaced by a scalar wave equation and polarisation effects are absent.

Using the above techniques we obtain, for N isotropic scalar point scatterers in vacuum positioned at $\{\boldsymbol{x}_n\}$, for the total T-matrix

$$T^{(N)}(z) = -\frac{t(z)}{4\pi} \sum_{n,m}^{N} |\boldsymbol{x}_n\rangle D^{-1}_{nm}(z) \langle \boldsymbol{x}_m|. \tag{2.1}$$

Here z is the complex energy, $|\mathbf{0}\rangle t(z) \langle \mathbf{0}|$ is the one-scatterer T-matrix. If for convenience we define $s \equiv z\,\mathrm{sign}(\mathrm{Im}\, z)$, it follows that $s^2 = z^2$, $\mathrm{Im}\, s > 0$ and

$$t(z) = \frac{-4\pi s^2}{1/\alpha - \mathrm{i}s^3} \tag{2.1a}$$

and $\mathbf{D}(z) \in \mathbb{C}^{N,N}$

$$D_{nm}(z) = \delta_{nm} - (1 - \delta_{nm})\, t(z) g(z, \boldsymbol{x}_n - \boldsymbol{x}_m). \tag{2.1b}$$

The constant α is a free parameter to be specified later. The empty-space Green function is

$$g(z, x) = -\frac{\exp(\mathrm{i}sx)}{4\pi x}. \tag{2.1c}$$

The scattering amplitude is

$$f(\boldsymbol{k} \to \boldsymbol{k}') = (2\pi)^3 \langle \boldsymbol{k}|\, T(k_0 + \mathrm{i}\epsilon)\, |\boldsymbol{k}'\rangle \tag{2.1d}$$

where $|\boldsymbol{k}| = |\boldsymbol{k}'| \equiv k_0$, which means that the total T-matrix is to be taken on the shell. For the Rayleigh point scatterers equation (2.1) also applies, but now

$$t(z) = \frac{-4\pi s^2}{1/\alpha - \frac{2}{3}\mathrm{i}s^3} \tag{2.2a}$$

and $\mathbf{D}(z) \in \mathbb{C}^{N,N} \otimes \mathbb{C}^{3,3}$

$$\mathbf{D}_{nm}(z) = \delta_{nm}\mathbf{I} - (1-\delta_{nm})t(z)\,\boldsymbol{g}(z, \boldsymbol{x}_n - \boldsymbol{x}_m). \tag{2.2b}$$

The empty-space Green function for the vector case is

$$\boldsymbol{g}(z, \boldsymbol{x}) = P(s\boldsymbol{x})\boldsymbol{\Delta}_{\boldsymbol{x}} + Q(s\boldsymbol{x})\,\hat{\boldsymbol{x}}\hat{\boldsymbol{x}} \tag{2.2c}$$

where the transverse part P and the longitudinal part Q are given by

$$P(y) = \frac{s}{4\pi}\left(-1 + \frac{1}{\mathrm{i}y} + \frac{1}{y^2}\right)\frac{\exp(\mathrm{i}y)}{y} \qquad Q(y) = -2\frac{s}{4\pi}\left(\frac{1}{\mathrm{i}y} + \frac{1}{y^2}\right)\frac{\exp(\mathrm{i}y)}{y}. \tag{2.2d}$$

The matrices $\boldsymbol{\Delta}_{\boldsymbol{x}}$ and $\hat{\boldsymbol{x}}\hat{\boldsymbol{x}}$ are projections perpendicular to and along the direction of $\boldsymbol{x}$, respectively. $\mathbf{I}$ is the 3×3 unit matrix. We infer that the T-matrix depends on the complex energy via $z\,\mathrm{sign}(\mathrm{Im}\,z)$. In sharp contrast with Schrödinger, we can identify two 'physical sheets', that cannot be connected by analytical continuation, because there is a continuous spectrum along both the positive and the negative real axis. The Green function in equation (2.2*c*) lacks, as mentioned earlier, square integrability. Note that the integral of the Green function itself does exist, provided we first integrate over angles. In fact, averaging over angles brings us back to the scalar Green function in equation (2.1*c*)

$$\int \frac{\mathrm{d}\hat{\boldsymbol{x}}}{4\pi}\boldsymbol{g}(z, \boldsymbol{x}) = \tfrac{2}{3}g(z, x)\,\mathbf{I}. \tag{2.2e}$$

The scattering amplitude is

$$f(k\boldsymbol{e}_{\boldsymbol{k}} \to k'\boldsymbol{e}'_{\boldsymbol{k}'}) = (2\pi)^3\,\langle \boldsymbol{k}|\boldsymbol{e}_{\boldsymbol{k}} \cdot \boldsymbol{T}(k_0 + \mathrm{i}\epsilon) \cdot \boldsymbol{e}'_{\boldsymbol{k}'}|\boldsymbol{k}'\rangle. \tag{2.2f}$$

The (normalised) polarisation vectors are denoted by $\boldsymbol{e}_{\boldsymbol{k}}$ and $\boldsymbol{e}'_{\boldsymbol{k}'}$, and again $|\boldsymbol{k}| = |\boldsymbol{k}'| \equiv k_0$. The T-matrix equation (2.2) is a tremendous simplification of the rigorous T-matrix in [15]. The one-scatterer albedo is defined as the ratio of the total scattering cross section and the imaginary part of the forward amplitude [16]. For our models

$$a_{\mathrm{s}} = \frac{-|t(k_0)|^2}{(4\pi/k_0)\mathrm{Im}\,t(k_0)} \tag{2.3a}$$

$$a_{\mathrm{R}} = \frac{-\frac{2}{3}|t(k_0)|^2}{(4\pi/k_0)\mathrm{Im}\,t(k_0)}. \tag{2.3b}$$

If the coupling parameter α is real, it follows from equations (2.1*a*) and (2.2*a*) that the albedo is unity. This is the *optical theorem* [17]. From now on we shall adopt conservative scattering and equation (2.3) applies. Most effective scattering occurs at resonance where $\alpha \to \infty$. Then the total cross section is proportional to λ^2/π, with λ the wavelength. Scatterers with *optical* volumes larger then their *physical* volumes are expected to be well approximated by point interaction models.

3. Renormalisation of the amplitude Green function

In this section we deal with dependent-scattering effects in the amplitude Green function, and show that the use of point scatterers allows a rigorous solution. Density corrections to the scattering mean free path were discussed by Bringi *et al* [18], who applied the rigorous Waterman formalism [17] and included a physical exclusion principle. For the actual calculation they had to rely on a 'quasi-crystalline approximation' which, in fact, neglects repeated scattering between scatterers. This is justified if the particles scatter predomimantly in the forward direction, as is the case for Mie spheres large compared to the wavelength, but not if the phase function is essentially isotropic. This is true for our point interaction models.

For the description of random media we are interested in an ensemble average of scattering quantities in a thermodynamic limit $N \to \infty, V \to \infty$ and $N/V \to n$. We will not deal with the important question whether or not this limit exists mathematically. Furthermore, no correlation effects are assumed and every configuration of the N scatterers is equally probable. This is clearly an oversimplification for large packing fractions, but we emphasise that physical exclusion can be neglected if the optical volume of the scatterer is larger than its 'hard-sphere radius'. Equation (2.1) gives rise [19] to the definition of a renormalised Green function G and a self-energy operator Σ that relates the latter to the empty-space Green function g. In operator notation

$$G(z) = g(z) + g(z)\Sigma(z)G(z) \tag{3.1}$$

with an analogous equation for the vector case. If we assume space to be translationally symmetric, equation (3.1) has a simple solution as, in reciprocal space, every operator is diagonal: $\langle \boldsymbol{p}|M|\boldsymbol{p}'\rangle = M(\boldsymbol{p})\delta(\boldsymbol{p}-\boldsymbol{p}')$. For the scalar case it follows that

$$G(z,\boldsymbol{p}) = \left[z^2 - p^2 - \Sigma(z,\boldsymbol{p})\right]^{-1} \tag{3.2a}$$

and for vector scattering that

$$\boldsymbol{G}(z,\boldsymbol{p}) = \left[z^2 - p^2\boldsymbol{\Delta}_{\boldsymbol{p}} - \boldsymbol{\Sigma}(z,\boldsymbol{p})\right]^{-1} \tag{3.2b}$$

where $\boldsymbol{\Delta}_{\boldsymbol{p}} \equiv \mathbf{I} - \hat{\boldsymbol{p}}\hat{\boldsymbol{p}}$ is the transverse projection matrix. The self-energy $\boldsymbol{\Sigma}(z,\boldsymbol{p})$ is now a 3×3 complex matrix. The usual independent-scattering approximation consists of taking the lowest order in density in the self-energy

$$\Sigma^{(1)}(z,\boldsymbol{p},\boldsymbol{p}') = (2\pi)^{-3}\left\langle \sum_{j=1}^{N} \exp(\mathrm{i}(\boldsymbol{p}\cdot\boldsymbol{x}_j))t(z)\exp(-\mathrm{i}(\boldsymbol{p}'\cdot\boldsymbol{x}_j))\right\rangle = nt(z)\delta(\boldsymbol{p}-\boldsymbol{p}'). \tag{3.3}$$

The ensemble-averaging is denoted by the brackets. For the vector case an extra identity $\mathbf{I} \in \mathbb{C}^{3,3}$ comes in. We take $z \equiv k_0 + \mathrm{i}\epsilon$, as in section 2. This choice makes equation (3.2) the definition of the *retarded* Green functions. From now on we shall omit the explicit z-dependence. Equation (3.3) gives rise to a new complex wavenumber

$$z^2 = (k_0 + \mathrm{i}\epsilon)^2 - nt.$$

In the low-density limit, the imaginary part directly relates to the scattering mean free path

$$\bar{l}_0^{-1} = -n\frac{\mathrm{Im}\, t}{k_0} = \begin{cases} n|t|^2/4\pi & \text{(scalar)} \\ n|t|^2/6\pi & \text{(vector)} \end{cases} \equiv n\sigma_s(k_0). \tag{3.4}$$

The second equality applies for conservative scatterers and follows from (2.3). We define the disorder parameter

$$\eta = 4\pi n/k_0^3. \tag{3.5}$$

Dependent-scattering corrections in the self-energy are shown in figure 1. For the scalar point interaction they sum [20] up to

$$\Sigma^{(2)}(p) = n^2 t^3 \int \mathrm{d}^3\boldsymbol{x}\, \frac{g^2(x)}{1-t^2g^2(x)} + n^2t^4 \int \mathrm{d}^3\boldsymbol{x}\, \frac{g^3(x)}{1-t^2g^2(x)} \exp(\mathrm{i}\boldsymbol{p}\cdot\boldsymbol{x}). \tag{3.6}$$

The first term represents the set of proper diagrams with the same scatterer at both sides (loops) and gives a dependent-scattering correction to the one-scatterer T-matrix, the second term the set with different scatterers at both sides and is, for point scatterers, the first p-dependent contribution. Its first order is subject to an ultraviolet (UV) singularity that is renormalised by adding the total geometric series. This contribution has an oscillatory behaviour near $p = 3k_0$, which is damped if the free-space Green functions in equation (3.6) are replaced by their averaged equivalent given in equation (3.2). Because of equation (3.2*a*), large values for p/k_0 are not important as long as $\Sigma(p)$ remains finite. Therefore we shall evaluate this contribution on the shell: $p = k_0$. This clears the way for solving the renormalisation issue. We propose the following (self-consistent) calculation scheme: first we replace every T-matrix by its loop-corrected value, and second we replace every Green function by its averaged equivalent according to equation (3.1). Of course we must be careful not to double count certain diagrams. This yields the following set of coupled equations

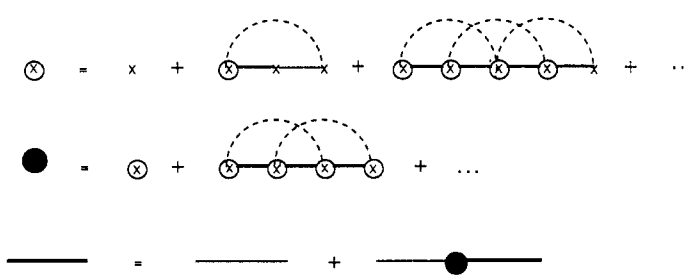

(3.7)

and was solved for various disorders using a Newton–Raphson method. In equation (3.7), the conventions are as in figure 1. A cross within a circle denotes the loop-corrected one-scatterer T-matrix; a bold line represents the renormalised Green function. The full circle is the self-energy operator. The third equation is Dyson's equation relating the renormalised Green function to the empty-space Green function. The scattering quantities of interest follow from the relation

$$k_0^2 - \Sigma(k_0) \equiv [k + (\mathrm{i}/2\bar{l})]^2. \tag{3.8}$$

The result for the scalar point scatterers is shown in figure 2(a). We have set the scatterers to resonance. For less effective scatterers, dependent-scattering corrections are strongly suppressed and we expect the independent-scattering approximation to become better. Near $\eta = 1$ the scattering mean free path becomes an *increasing* function of density. We infer that $k\bar{l} > 1$ for all disorders. For $\eta > 1.36$ the iteration procedure no longer converged in less than ten iterations.

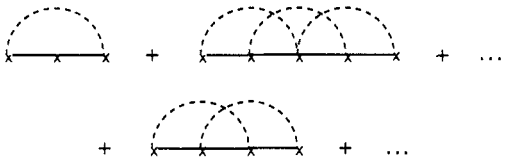

Figure 1. Dependent-scattering corrections to the self-energy. A straight line represents the empty-space Green function; broken lines are connections between identical scatterers. A cross denotes the one-scatterer T-matrix.

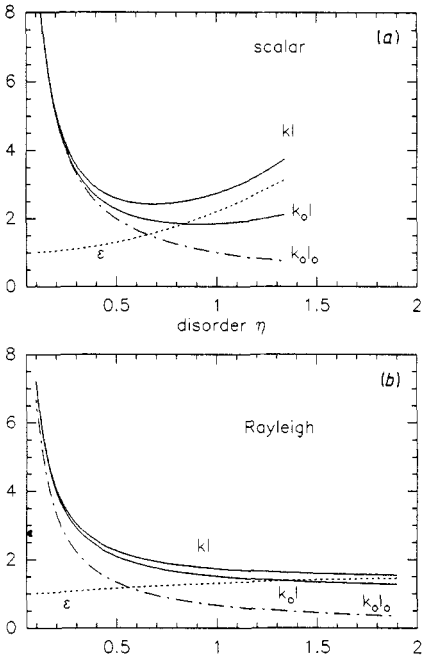

Figure 2. Various scattering quantities following from the solution of the self-consistent equation (3.7): k_0 is the empty-space wavenumber, k is the renormalised wavenumber and $\epsilon \equiv k^2/k_0^2$ is the dielectric constant, $\bar{l}_0$ is the independent-scattering result for the scattering mean free path; $\bar{l}$ is the scattering mean free path including dependent-scattering corrections. (a) Scalar isotropic point scatterers at resonance; (b) vector Rayleigh point scatterers at resonance.

For the Rayleigh point scatterer the calculation is essentially the same. Using equation (2.2c) the two-scatterer correction to the self-energy is

$$\boldsymbol{\Sigma}^{(2)}(\boldsymbol{p}) = \Sigma_i^{(2)}(p)\mathbf{I} + \Sigma_a(p)\hat{\boldsymbol{p}}\hat{\boldsymbol{p}}$$

$$\Sigma_i^{(2)}(p) = n^2 t^3 \int \mathrm{d}^3\boldsymbol{x} \left(\frac{2}{3} \frac{P^2}{1-t^2P^2} + \frac{1}{3} \frac{Q^2}{1-t^2Q^2} \right) + n^2 t^4 \int \mathrm{d}^3\boldsymbol{x} \left[\left(j_0(px) - \frac{j_1(px)}{px} \right) \frac{P^3}{1-t^2P^2} + \frac{j_1(px)}{px} \frac{Q^3}{1-t^2Q^2} \right]$$

$$\Sigma_a(p) = n^2 t^4 \int \mathrm{d}^3\boldsymbol{x}\, j_2(px) \left(\frac{P^3}{1-t^2P^2} - \frac{Q^3}{1-t^2Q^2} \right). \tag{3.9}$$

The Green function in reciprocal space becomes, according to equation (3.2*b*)

$$\boldsymbol{G}(\boldsymbol{p}) = \frac{\boldsymbol{\Delta}_{\boldsymbol{p}}}{k_0^2 - p^2 - \Sigma_i(p)} + \frac{\hat{\boldsymbol{p}}\hat{\boldsymbol{p}}}{k_0^2 - \Sigma_i(p)} + \frac{\Sigma_a(p)}{[k_0^2 - \Sigma_i(p)]\,[k_0^2 - \Sigma_i(p) - \Sigma_a(p)]} \hat{\boldsymbol{p}}\hat{\boldsymbol{p}} \tag{3.10}$$

where $\Sigma_i(p) \equiv nt(k_0) + \Sigma_i^{(2)}(p)$. The p-dependent contribution $\Sigma_i^{(2)}(p)$ turns out to be rather weakly dependent on p, being finite for both small and large values of p. It will therefore be evaluated on-shell: $p = k_0$. For $\Sigma_a(p)$ things are different as it finds itself in the nominator of equation (3.10).

Transforming to real space yields the following averaged Green function

$$\boldsymbol{G}(\boldsymbol{x}) = g(k_0 \to z, \boldsymbol{x}) + \frac{1}{z^2} \int \frac{\mathrm{d}^3\boldsymbol{p}}{(2\pi)^3} \frac{\Sigma_a(p)}{z^2 - \Sigma_a(p)} \hat{\boldsymbol{p}}\hat{\boldsymbol{p}} \exp(\mathrm{i}\boldsymbol{p}\cdot\boldsymbol{x}). \tag{3.11}$$

We have defined $z^2 \equiv k_0^2 - \Sigma_i(k_0)$. Two comments are in order here. Firstly, the x^{-3} singularity of the vector Green function does not give UV problems in the self-energy because the full series is summed. In fact the problems occur when $t \to 0$. In that case the integrands of equation (3.9) have a pole at $kx_r \approx (kt/4\pi)^{1/3}$ approaching the real axis. Physically this pole reflects a standing wave between two scatterers. If we fit the T-matrix to a small Mie sphere with radius a and dielectric constant $\epsilon > 1$ then $t \approx (4\pi/k)(ka)^3\,(\epsilon-1)/(\epsilon+2)$ and hence $x_r < a$. Thus, this resonance is not present in a scattering event involving two identical small Mie spheres.

Secondly, the two-scatterer renormalisation not only gives a damped wave vector, but also adds an extra term to the averaged Green function. Appendix C shows that this term is in fact an exponentially damped longitudinal mode with decay length $\bar{l}/3$. It is dropped in the numerical calculations, although it may contribute for large disorders. The results for the scattering mean free path and the dielectric constant are shown in figure 2(*b*). The mean free path is now found to decay with density, but we see that the condition $k\bar{l} < 1$ is never reached. Obviously, dependent-scattering effects increase the scattering mean free path; this conclusion remains true if the scatterers are set off resonance. The saturation for large disorders is due to the very singular Green function as the argument x becomes much smaller than the wavelength:

$$\boldsymbol{G}(\boldsymbol{x}) \to \frac{\mathbf{I} - 3\hat{\boldsymbol{x}}\hat{\boldsymbol{x}}}{4\pi z^2 x^3}. \tag{3.12}$$

Using the solution of the self-consistent equation (3.7) it is possible to compute the self-energies in equation (3.9) for any momentum p. This allows a check on the on-shell approximation. The self-energies are plotted in figure 3, for various disorders. We can infer that setting $\Sigma_i(p)$ on the shell is rather accurate. The self-energy appearing in the

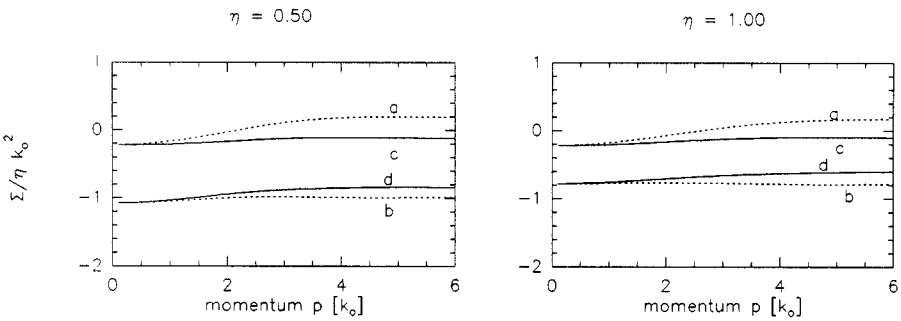

Figure 3. The self-energy for the Rayleigh point scatterers as a function of momentum, for various disorders, using the solution of the self-consistent equation (3.7). This equation was solved by setting the self-energy Σ_i on the shell: $p = k_0$ and the one-scatterer T-matrix to resonance. The bold lines denote $\Sigma_i(p)$; the broken lines $\Sigma_i(p) + \Sigma_a(p)$. a, $\mathrm{Re}[\Sigma_i + \Sigma_a]$; b, $\mathrm{Im}[\Sigma_i + \Sigma_a]$; c, $\mathrm{Re}\,\Sigma_i$ and d, $\mathrm{Im}\,\Sigma_i$. The independent-scattering result is: $\Sigma_i/\eta k_0^2 = -1.5i$.

denominator of the integrand in equation (3.10) is more dependent on the momentum because $\Sigma_a(p) \sim p^2$ as $p \to 0$.

The change in the scattering mean free path in lowest order of the density is found from equation (3.8)

$$\frac{\bar{l}}{\bar{l}_0} = 1 - \left(\frac{1}{2}\frac{\mathrm{Re}\,\Sigma^{(1)}(k_0)}{k_0^2} + \frac{\mathrm{Im}\,\Sigma^{(2)}(k_0)}{\mathrm{Im}\,\Sigma^{(1)}(k_0)}\right) + \mathcal{O}(\eta^2). \tag{3.13}$$

The correction is still a function of the one-scatterer T-matrix, and can be calculated easily from equation (3.6) for scalar point scatterers, and from (3.9) for Rayleigh point scatterers. For the special case where the scatterers are at resonance, we find for the scalar point scatterers that

$$\bar{l}/\bar{l}_0 = 1 - 0.375\eta \tag{3.14a}$$

and for the Rayleigh point scatterers that

$$\bar{l}/\bar{l}_0 = 1 + 0.427\eta. \tag{3.14b}$$

Clearly, in lowest order of the density, and at resonance, dependent-scattering corrections increase extinction for scalar scatterers, and decrease extinction for Rayleigh scatterers. This involves a redistribution of energy. We will not deal with the energy balance in case dependent-scattering effects are incorporated.

4. New coherent effects in the scattered intensity

The usual approach to calculate the scattered intensity from a slab containing randomly distributed isotropic point scatterers [1, 21] is to solve the Milne equation. This equation follows from perturbation theory if the independent-scattering approximation is used for the scattering mean free path and under the assumption that the multiple scattered light is given by the ladder diagrams only. This simplification is

usually referred to as the first-order smoothing method [19] and involves neglect of all high orders in density. After first-order smoothing, the Ward identity [8,22], which is a rigorous identity relating self-energy and irreducible vertex by energy- (or particle-) conservation, is still satisfied and reduces to equation (3.4). The Milne equation conserves, therefore, energy. The most important coherent effect is described by the time-reversed variants of the ladder sum. They account for a *narrow* cone at backscattering with angular width $\Delta\theta \approx 1/k\bar{l}$. Its exact angular dependence is well understood on the basis of a generalised Milne equation [2], although a diffusion approximation usually suffices.

A rigorous multiple-scattering theory for Rayleigh vector point scatterers has not yet been developed, and one must rely on a diffusion approximation [4,5]. There is one important reason why the diffusion approximation is not satisfactory. Because it is essentially a long light path limit, short light paths are strongly underestimated. Consequently, the diffusion approximation predicts the wrong angular dependence in the wings of the enhanced backscattering cone ($\theta > 1/k\bar{l}$) where low orders of scattering dominate. Moreover, it is known that low orders have a strong tendency to preserve polarisation [6] and thus we cannot expect the diffusion approximation to account for observed polarisation effects in the backscattering of vector waves.

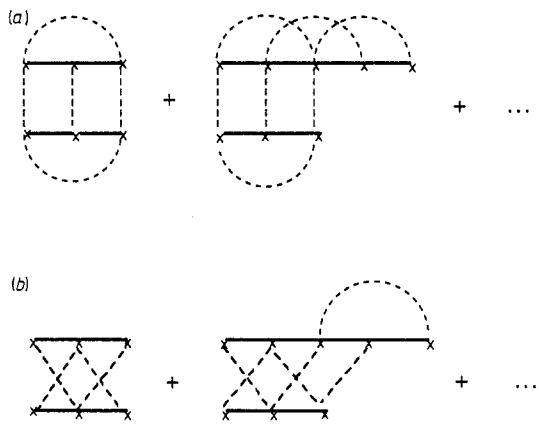

Figure 4. (*a*) Intensity loop diagrams involving two scatterers. A bold line corresponds to the renormalised Green function. (*b*) Forward-crossed diagrams involving two scatterers. They give constructive interference at forward scattering and are in that case equal to the loop background.

This section deals with the calculation of low-order scattering events which can, using the point scattering models, be calculated analytically. We will discuss the two-scatterer ladder and the two-scatterer most-crossed diagram, and, in addition, more complicated two-scatterer events such as loops. The scattered intensity will be expressed by means of the bistatic coefficient [21]. This is a dimensionless quantity that is easily accessible to experiments. For the Rayleigh point scatterer the two-scatterer intensity loops, shown diagrammatically in figure 4(*a*), contribute to the bistatic coefficient at exactly backscattering

$$\gamma_{\mathcal{L}(2)} = \left(\frac{A}{4\pi}\right)^{-1} \frac{n^2|t|^6}{(4\pi)^2} \int_{\text{slab}} \mathrm{d}^3\boldsymbol{x}_1 \int_{\text{slab}} \mathrm{d}^3\boldsymbol{x}_2 \, |\mathcal{L}(\boldsymbol{x}_{12})|^2 \exp(-2z_1/\bar{l}) \quad (4.1)$$

where the loop kernel is

$$\mathcal{L}(\boldsymbol{x}) = \boldsymbol{e}_{\boldsymbol{k}} \cdot \boldsymbol{G}^2(\boldsymbol{x}) \cdot \left[1 - t^2 \boldsymbol{G}^2(\boldsymbol{x})\right]^{-1} \cdot \boldsymbol{e}'_{\boldsymbol{k}'}$$

A is the illuminated surface of the slab, and t given by equation (2.2a). We have chosen the z axis perpendicular to the slab along the direction of the incoming wave; $\boldsymbol{G}(\boldsymbol{x})$ is the averaged Green function defined in equation (3.11). The bistatic coefficient is still a function of the slab thickness, the density of the scatterers, and their T-matrix t. To get some physical insight, let us assume $k\bar{l} \gg 1$. As the kernel falls off rapidly with distance ($|\mathcal{L}|^2 \sim \exp(-2x_{12}/\bar{l})/x_{12}^4$), we shall rely on the 'infinite space approximation' and integrate the position of the second scatterer over all of space. After some algebra we find, using equation (3.4) and the disorder parameter in equation (3.5), that

$$\gamma_{\mathcal{L}(2)} = \tfrac{3}{4}\eta|\tilde{t}|^4 \left[1 - \exp(-2\tau)\right] \mathcal{G}(\tilde{t}, \boldsymbol{e}_{\boldsymbol{k}} \cdot \boldsymbol{e}'_{\boldsymbol{k}'}) \tag{4.2}$$

where

$$\mathcal{G}(\tilde{t}, \varpi) = \int_0^\infty \mathrm{d}y\, y^2 \left(|T-1|^2 \varpi^2 + \frac{1+2\varpi^2}{15} |R-T|^2 + \frac{2}{3}\varpi^2 \mathrm{Re}(T-1)(R-T)^* \right).$$

In this equation we have introduced the dimensionless quantities $\tilde{t} \equiv (4\pi/k_0)^{-1} t$, the optical depth of the slab τ and

$$T = \frac{1}{1 - t^2 P^2} \qquad R = \frac{1}{1 - t^2 Q^2}.$$

It can be solved numerically for any allowed value of the one-scatterer T-matrix t. At resonance this yields

$$\gamma_{\mathcal{L}(2)} = \eta[1.41 + 6.52(\boldsymbol{e}_{\boldsymbol{k}} \cdot \boldsymbol{e}'_{\boldsymbol{k}'})^2][1 - \exp(-2\tau)] \tag{4.2a}$$

This is to be taken as an upper limit for the contribution of these loops at backscattering, and can be compared to the single-scattering bistatic coefficient

$$\gamma_{\mathrm{s}} = \tfrac{3}{4}(\boldsymbol{e}_{\boldsymbol{k}} \cdot \boldsymbol{e}'_{\boldsymbol{k}'})^2 [1 - \exp(-2\tau)]. \tag{4.3}$$

For $\eta \approx 0.1$, the contribution of these loops is thus comparable to single scattering, and has, in addition, a cross-polarised component. It is seen that they scale with a first power of the density. As we will see in section 5, this is not true for loops involving more than two scatterers. The bistatic coefficient has, judging from its optical depth dependence, a penetration depth $\bar{l}$ like the one for single-scattering. Therefore, the two-scatterer loops cannot be responsible for a change in the enhanced backscattering factor in weak localisation experiments on *difference* slabs (e.g. slabs for which the contribution of the first few mean free paths has been subtracted): it gives renormalised single scattering and a slight change in its degree of polarisation.

The total two-scatterer ladder sum is illustrated in figure 5(a). They contribute in the backward direction

$$\gamma_{L(2)} = \left(\frac{A}{4\pi}\right)^{-1} \frac{n^2|t|^4}{(4\pi)^2} \iint \mathrm{d}^3\boldsymbol{x}_1\, \mathrm{d}^3\boldsymbol{x}_2\, |L(\boldsymbol{x}_{12})|^2 \exp\left(-\frac{z_1 + z_2}{\bar{l}}\right) \tag{4.4}$$

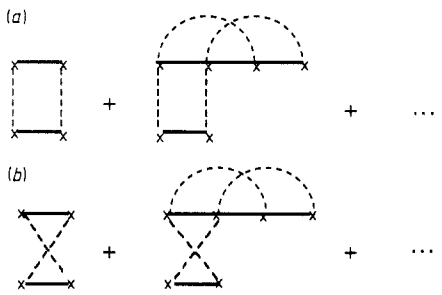

Figure 5. (*a*) The two-scatterer ladders including dependent-scattering corrections. (*b*) The two-scatterer backward crossed diagrams. They are the time-reversal variants of the two-scatterer ladders and give constructive interference in the backward direction.

where the ladder kernel is

$$L(\boldsymbol{x}) = \boldsymbol{e}_{\boldsymbol{k}} \cdot \boldsymbol{G}(\boldsymbol{x}) \cdot \left[1 - t^2 \boldsymbol{G}(\boldsymbol{x})^2\right]^{-1} \cdot \boldsymbol{e}'_{\boldsymbol{k}'}.$$

It is important to note that, because of the singular nature of the vector Green function, the incoherent ladder (first diagram of figure 5(*a*)) suffers from an UV singularity. Only in the limit $k\bar{l} \to \infty$ do the singular terms disappear. Scaling with $k\bar{l}$ gives in that case the ladder kernel in the far-field approximation

$$|L_\infty(\boldsymbol{x})|^2 = \frac{1}{x^2} \exp(-x/\bar{l}) \left(\boldsymbol{e}_{\boldsymbol{k}} \cdot \boldsymbol{\Delta}_{\boldsymbol{x}} \cdot \boldsymbol{e}'_{\boldsymbol{k}'}\right)^2. \tag{4.5}$$

The bistatic coefficient becomes, in the co-polarised ($\boldsymbol{e}_{\boldsymbol{k}} \parallel \boldsymbol{e}'_{\boldsymbol{k}'}$) and cross-polarised ($\boldsymbol{e}_{\boldsymbol{k}} \perp \boldsymbol{e}'_{\boldsymbol{k}'}$) channel

$$\begin{aligned}
\lim_{k\bar{l}\to\infty} \begin{pmatrix} \gamma_{L(2)}(\text{co-pol}) \\ \gamma_{L(2)}(\text{cross}) \end{pmatrix} &= \frac{9}{8}\left[1 - \exp(-2\tau)\right] \int_0^1 \mathrm{d}c \left[c^2 \begin{pmatrix} 1 \\ 0 \end{pmatrix} + (1-c^2)^2 \begin{pmatrix} \frac{3}{8} \\ \frac{1}{8} \end{pmatrix}\right] \\
&\quad \times \frac{1}{1+c}\left[1 - \exp(-(1+c)\tau)\right] \\
&\overset{\tau \gg 1}{=} \frac{9}{8} \begin{pmatrix} \log 2 - \frac{11}{32} \\ \frac{5}{96} \end{pmatrix} \\
&= \begin{pmatrix} 0.3930 \\ 0.0586 \end{pmatrix}.
\end{aligned} \tag{4.6}$$

The co-polarised value compares well to the scalar two-scatterer ladder $\frac{1}{2}\log 2 = 0.3466$. Whereas single-scattering equation (4.3) is 100% polarised, the two-scatterer contribution has a degree of polarisation

$$\frac{\gamma(\text{co-pol}) - \gamma(\text{cross})}{\gamma(\text{co-pol}) + \gamma(\text{cross})} = 74\%.$$

Assuming that the two-scatterer ladder, summed for both channels, amounts to about 8% of the total incoherent background at backscattering, which is true for scalar isotropic scattering [2], we can deduce that single and double scattering events are

responsible for a polarisation degree roughly equal to 18% of the backscattered signal. This is not far different from the value 24% found in [7] by numerical simulation, confirming that the partial polarisation of the backscattered signal is due to the very low orders of scattering.

Near-field corrections to the two-scatterer ladder diagram can be found, for any disorder, by subtracting equation (4.6) from equation (4.4). In the limit of weak disorder $k\bar{l} \gg 1$ we find that

$$\Delta\gamma_{L(2)} = \Delta\gamma(\text{trans.}) + \Delta\gamma(\text{long.}) + \Delta\gamma(\text{trans./long.}) \tag{4.7a}$$

where

$$\Delta\gamma(\text{trans.}) = \frac{3}{4}\eta|\tilde{t}|^2 \begin{pmatrix} 8/15 \\ 1/15 \end{pmatrix} \int_0^\infty \mathrm{d}y\, y^2 \left(|\tilde{P}T|^2 - \frac{1}{y^2} \right)$$

$$\Delta\gamma(\text{long.}) = \frac{3}{4}\eta|\tilde{t}|^2 \begin{pmatrix} 1/5 \\ 1/15 \end{pmatrix} \int_0^\infty \mathrm{d}y\, y^2 |\tilde{Q}R|^2$$

$$\Delta\gamma(\text{trans./long.}) = \frac{3}{4}\eta|\tilde{t}|^2 \begin{pmatrix} 2/15 \\ -1/15 \end{pmatrix} \int_0^\infty \mathrm{d}y\, y^2 2\mathrm{Re}\left[\tilde{Q}R(\tilde{P}T)^* \right].$$

We have defined $\tilde{P}, \tilde{Q} \equiv (4\pi/k_0)P(y), Q(y)$. Again, the upper number of the column vector applies in the co-polarised channel , and the lower number in the cross-polarised channel. The integrals can be evaluted numerically for any one-scatterer T-matrix. Setting this T-matrix to resonance we find that

$$\Delta\gamma_{L(2)} = \begin{pmatrix} -1.36 \\ 0.190 \end{pmatrix} \eta. \tag{4.7b}$$

Note that we deal here with a *positive* correction to the enhanced backscattering factor in the co-polarised channel, because the background is decreased.

The time-reversed variants of the two-scatterer ladders (figure 5(b)) give the lowest order contribution to the backward cone. Assuming again $k\bar{l} \to \infty$, we deduce, as a function of the backscattering angle θ

$$\gamma_{C(2)}(\boldsymbol{k}, \boldsymbol{k}') = \left(\frac{A}{4\pi} \right)^{-1} \frac{n^2|t|^4}{(4\pi)^2} \int_{\text{slab}} \mathrm{d}^3\boldsymbol{x}_1 \int_{\text{slab}} \mathrm{d}^3\boldsymbol{x}_2\, |L_\infty(\boldsymbol{x}_{12})|^2$$
$$\times \exp\left[-s(\theta) \left(\frac{z_1 + z_2}{\bar{l}} \right) \right] \cos \boldsymbol{b} \cdot \boldsymbol{x}_{12} \tag{4.8}$$

with $\boldsymbol{b} \equiv \boldsymbol{k} + \boldsymbol{k}'$ and $s(\theta) \equiv \frac{1}{2}(1 + 1/\cos\theta)$. In appendix A this equation is further analysed in the regime where it is of experimental importance, namely in the wings: $\theta > (k_0\bar{l}_0)^{-1}$. It will be shown that equation (4.8) accounts for a θ^{-1} fall-off in the co-polarised channel of the cone, and a θ^{-2} fall-off in the cross-polarised channel. In addition, polarisation effects in the co-polarised channel can be understood quantitatively, and confirm the qualitative analysis in [6]. As a corollary we calculated the wings for circularly polarised light in both helicity channels. We find that both channels exhibit θ^{-1} behaviour, and are isotropic, like the wings for scalar waves.

Near-field corrections to the two-scatterer cone can be found as follows:

$$\Delta\gamma_{C(2)}(\boldsymbol{k},\boldsymbol{k}') = \tfrac{3}{2}\eta|\tilde{t}|^2 \frac{1}{(\cos\theta)^{-1}+1}\int \frac{\mathrm{d}^3\boldsymbol{y}}{4\pi}\left[|L(\boldsymbol{y})|^2 - |L_\infty(\boldsymbol{y})|^2\right]\cos\boldsymbol{b}\cdot\boldsymbol{y}. \tag{4.9}$$

We have neglected some extinction factors, because the integral exists without them. Physically this means that the angular width of this correction is by no means equal to the typical $(k\tilde{l})^{-1}$ predicted by the most-crossed diagrams in the far-field approximation. Whereas the latter account for a large narrow cone the diagrams in equation (4.9) yield a small broad cone, and can better be classified as a density correction to the *background*. One should therefore be very careful with the statement that the enhanced backscattering factor is only influenced by angle-independent diagrams that are equal to their time-reversed equivalent or do not have a time-reversed equivalent at all.

The last two-scatterer intensity diagrams we will discuss are shown in figure 4(b). It is easy to see that these diagrams give constructive interference in the *forward* direction. Moreover, their value at exactly forward scattering is equal to the loop background. In fact, any forward-crossed diagram has a loop equivalent which is angle independent. The reverse statement is not true. The bistatic coefficient behind the slab is, in the infinite space approximation, as a function of the forward scattering angle θ

$$\gamma_{\mathcal{F}(2)}(\boldsymbol{k},\boldsymbol{k}') = \tfrac{2}{3}\eta|\tilde{t}|^4\left(\frac{\exp(-\tau)-\exp(-\tau/\cos\theta)}{(\cos\theta)^{-1}-1}\right)\int\frac{\mathrm{d}^3\boldsymbol{y}}{4\pi}|\mathcal{F}(\boldsymbol{y})|^2\cos\boldsymbol{f}\cdot\boldsymbol{y} \tag{4.10}$$

with

$$\mathcal{F}(\boldsymbol{y}) = (T-1)\boldsymbol{e}_{\boldsymbol{k}}\cdot\boldsymbol{e}'_{\boldsymbol{k}'} + (R-T)(\boldsymbol{e}_{\boldsymbol{k}}\cdot\hat{\boldsymbol{y}})(\boldsymbol{e}'_{\boldsymbol{k}'}\cdot\hat{\boldsymbol{y}})$$

and $\boldsymbol{f} = \boldsymbol{k} - \boldsymbol{k}'$. Because the integral exists for any θ without damping of the Green function, the angular width of this forward cone is not $(k\tilde{l})^{-1}$, but much wider and is mainly determined by the τ-dependent prefactor. This will complicate its verification in transmission experiments.

5. High-order loops and forward-crossed diagrams

We have seen that the loops involving two scatterers suffer from an UV singularity, scale with a first power in density, and have a coherent analogue in the forward direction. We will now study the loops and forward-crossed diagrams with more than two scatterers. Because of the complexity of these diagrams we will restrict our discussion to scalar isotropic point scatterers. It is shown in appendix B that the scalar loops involving three scatterers (figure 6(a)) are subject to a logarithmic singularity and must be renormalised. Physically this means that loops shorter than λ are excluded because the optical volumes of the scatterers start to overlap. Consequently, their contribution to the bistatic coefficient at backscattering has a logarithmic density dependence. A numerical evaluation of equations (B.11) and (B.12) in appendix B resulted in the approximate expression, for scatterers at resonance in a semi-infinite slab, valid in the limit of small disorder $\eta \to 0$

$$\gamma_{\mathcal{L}(3)} \approx -1.95\eta^2\log(15.1\eta). \tag{5.1}$$

The loops involving four scatterers and more, 'diffusive loops', are shown in figure 6(*b*), and do no longer suffer from this UV singularity. Using the method of images [2,5], they can be calculated rigorously for any optical depth (appendix B). They are well approximated by the expressions

$$\gamma_{\mathcal{L}(n\geq 4)} \approx 2.60\eta^2|\tilde{t}|^6\,[1-\exp(-1.25\tau)] \tag{5.2a}$$

at backward scattering, and

$$\gamma_{\mathcal{L}(n\geq 4)} \approx 3.79\eta^2|\tilde{t}|^6\tau\exp(-0.85\tau). \tag{5.2b}$$

at forward scattering.

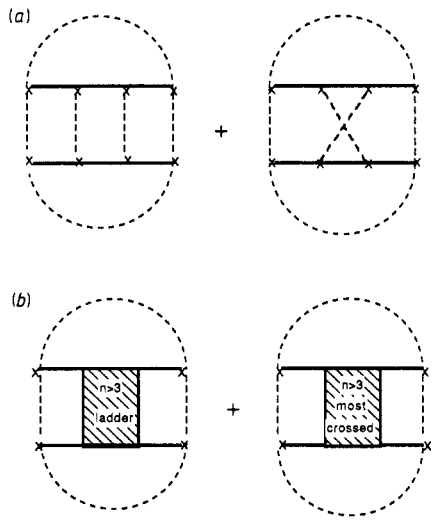

Figure 6. (*a*) Intensity loops involving three scatterers. Both diagrams give an equal angle-independent contribution. They are subject to a logarithmic singularity. (*b*) Diffusive loops, involving four or more scatterers. Again both diagrams give an equal angle-independent contribution, but do not suffer from an UV singularity.

Judging from equation (5.2), these loops have a penetration depth that is larger than $\bar{l}$ and as a result do not give renormalised single-scattering like the two-scatterer loops. The loops involving three or more scatterers have a coherent equivalent as well, but because of the complex irreducible nature of these high-order forward-crossed diagrams it is not straightforward to get an expression for them using the method of images. In order to find out whether or not these diagrams are responsible for a narrow forward cone, we will again rely on the 'infinite space approximation'. Appendix B shows that the angular dependence of the forward cone resulting from three scatterers has a logarithmic angle dependence and is therefore *not* narrow. For the coherent equivalents of the loops involving four or more scatterers it is found that

$$\gamma_{\mathcal{F}(n\geq 4)}(\theta) \approx \frac{4}{\pi}\eta^2|\tilde{t}|^6\tau\exp(-\tau)C(\boldsymbol{f}) \tag{5.3}$$

with

$$C(\boldsymbol{f}) = \int \frac{\mathrm{d}^3\boldsymbol{q}}{4\pi}\,\frac{A^2(q)A^2(|\boldsymbol{q}+\boldsymbol{f}|)}{1-A(|\boldsymbol{q}+\boldsymbol{f}|)}.$$

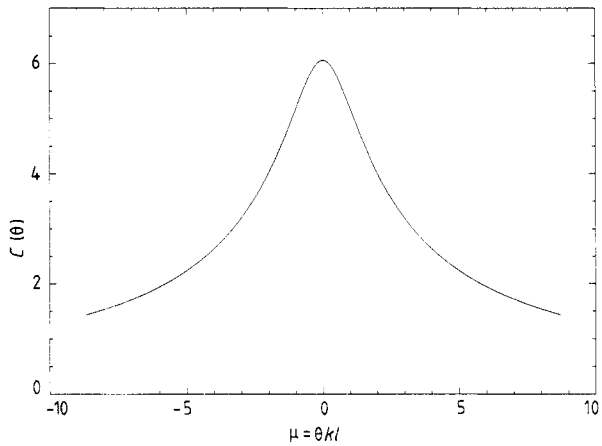

Figure 7. The function $C(\boldsymbol{f})$ given in equation (5.3). It gives the form of the forward cone resulting from scattering from four scatterers and more on the basis of the infinite space approximation and in the limit of weak scattering: $k\bar{l} \gg 1$. It is a rather smooth function of the forward-scattering angle θ and has angular width $3/k\bar{l}$.

We have defined $A(p) = \tan^{-1} p/p$ and $\boldsymbol{f} = \bar{l}_0 (\boldsymbol{k} - \boldsymbol{k}')$. Equation (5.3) is a very rough estimate because small q (long loops) suffer severely from the finiteness of the slab, but for $f = 0$, the exact numerical value is given by equation (5.2*b*). The function $C(\boldsymbol{f})$ is plotted in figure 7. We infer a forward cone with angular width $\Delta\theta \approx 3(k_0\bar{l}_0)^{-1}$. A very important difference between this forward cone and the backward cone is illustrated in equation (5.3). Whereas the enhanced backscattering is essentially a diffusion process with long light paths involving N scattering events being responsible for a small backscattering angle, according to $\Delta\theta \approx (k_0\bar{l}_0)^{-1}/N^{1/2}$, the physical picture for enhanced forward scattering is a recurrent random walk. The endpoints of the two interfering loops are roughly one steplength $\bar{l}$ apart, giving $\Delta\theta \approx (k\bar{l})^{-1}$, independent of the length of the loops. This fact makes the enhanced forward scattering less pronounced than enhanced backscattering. Recurrent light paths are strongly suppressed if the scatterers scatter predominantly in the forward direction, such as Mie spheres that are large compared to the wavelength.

Because of the scaling with η^2, and the exponential optical depth dependence of the bistatic coefficient, it will be very difficult to detect this enhanced forward scattering. It may be argued that this cone is also present in the cross-polarised channel for which detection is much easier. In this channel we expect no contribution from the attenuated incoming wave, nor from single scattering. Detection of this forward cone would be a unique direct verification of the very existence of recurrent light paths.

6. Concluding remarks and outlook

We have shown that, for large disorders, dependent-scattering corrections increase the scattering mean free path considerably. However, we have relied on an on-shell approximation for the self-energy and ignored pair correlations. A more exact analysis of the behaviour of the amplitude Green function for large disorders is clearly needed. We found that after renormalisation of the amplitude vector Green function, an extra longitudinal term arises which is of very short range. Although there are

experimental indications [2, 18] that the scattering mean free path becomes larger, for large packing fractions, than the independent-scattering result, one should realise that pair-correlation effects might play an important role as well.

It was found that two-scatterer intensity loops scale with a first power of the density after renormalisation and give a contribution to single-scattering. Therefore, they cannot be responsible for a change in the enhanced backscattering factor, especially not for difference slabs. Furthermore, we have indicated that longitudinal near-field terms cannot be neglected for large packing fractions. They were calculated for the two-scatterer ladder and most-crossed diagrams. It turned out that the latter do not contribute to enhanced backscattering as their cones are so wide that they can better be classified as background. Loops involving more than three scatterers penetrate deeper than $\bar{l}$ into the slab, and, thus, do not give renormalised single-scattering. Because of their second-order density dependence, they cannot account for a decrease of the enhanced backscattering factor.

It was shown that the loops have, just like the incoherent ladder diagrams, a coherent equivalent: the forward-crossed diagrams. For our point scatterers the lowest orders in density of the forward-crossed diagrams yield a broad cone. Orders of scattering larger than three give a narrow cone, but are typically a factor $k\bar{l}$ smaller. This makes the enhanced forward scattering very difficult to detect in weak localisation experiments. Experiments are going on at the University of Amsterdam to detect the forward cone in the cross-polarised channel, but have not yet verified its existence. Near the mobility edge we expect $k\bar{l} \approx 1$ and their *positive* contribution to the diffusion coefficient may no longer be negligible.

Finally, we have confirmed the existence of polarisation effects in the backscattered intensity of vector waves by an exact calculation of the contribution coming from the ladder and most-crossed diagram involving two Rayleigh vector point scatterers. These polarisation effects were already confirmed by experiments, and explained qualitatively. We indicated a *new* feature: for such scatterers the co-polarised wings of the enhanced backscattering cone exhibit a θ^{-1} fall-off, whereas the cross-polarised wings turn out to obey a θ^{-2} fall-off along the direction of one of the polarisation vectors. This is not predicted by the diffusion approximation.

Acknowledgments

This work is part of the research programme of the Stichting voor Fundamenteel Onderzoek der Materie (FOM) and was made possible by financial support from the Nederlandse Organisatie voor Wetenschappelijk Onderzoek (NWO).

Appendix A The wings of the two-scatterer cone

In the case of scalar backscattering from a semi-infinite slab, the two-scatterer cone is given by the bistatic coefficient

$$\gamma_{C(2)}(\boldsymbol{k}, \boldsymbol{k}') = \frac{k_0\bar{l}}{(k_0\bar{l}_0)^2} s(\theta) int \frac{\mathrm{d}^3\boldsymbol{y}}{4\pi} \frac{1}{y^2} \exp\left(-y/k_0\bar{l} - |z|s(\theta)/k_0\bar{l}\right) \cos \boldsymbol{b}\cdot\boldsymbol{y}$$

with $\boldsymbol{b} = k_0^{-1}(\boldsymbol{k} + \boldsymbol{k}')$, $b = 2\sin\theta/2$, and $s(\theta) = (1/\cos\theta + 1)^{-1}$. This integral can be solved numerically for any disorder. To get some physical insight, let us assume

weak disorder: $k_0\bar{l} = k_0\bar{l}_0 \gg 1$. In the wings we have, by definition, $b \gg (k_0\bar{l}_0)^{-1}$ and the bistatic coefficient simplifies to

$$\gamma_{C(2)}\left[\theta \gg (k_0\bar{l}_0)^{-1}\right] = (k_0\bar{l}_0)^{-1} s(\theta) \int_0^\infty \mathrm{d}y \frac{\sin by}{by} = (k_0\bar{l}_0)^{-1} s(\theta)\frac{\pi}{2} b^{-1}.$$

Defining $\mu \equiv \theta k_0\bar{l}_0$, and under the assumption that $\theta \ll 1$, we find that

$$\gamma_{C(2)}\left[\theta \gg (k_0\bar{l}_0)^{-1}\right] \approx \frac{\pi}{4}\mu^{-1} = 0.79\mu^{-1}. \tag{A.1}$$

This can be compared to the wings expected on the basis of the diffusion approximation [2,3]

$$\gamma_{C(\mathrm{diff.})}\left[\theta \gg (k_0\bar{l}_0)^{-1}\right] \approx \tfrac{3}{2}\mu^{-2}. \tag{A.2}$$

This is already less than equation (A.1) for $\mu \geq 2$. The μ^{-2} fall-off is a direct result of the adopted diffusion propagator. In the diffusion approximation, the rigorous (translationally symmetric) propagator for scalar isotropic point scatterers

$$D(q) = \frac{\tan^{-1} q/q}{1 - \tan^{-1} q/q} \tag{A.3a}$$

is approximated by its hydrodynamic limit $3/q^2$. Here q is the momentum transfer, scaled with the mean free path. We see that this approximation holds for large transfers, thus in the wings of the cone, as well, provided we 'drop' the first order, the two-scatterer contribution. Then

$$D^{(2)}(q) \equiv \frac{(\tan^{-1} q/q)^2}{1 - \tan^{-1} q/q} \begin{cases} \overset{q\to\infty}{\to} & 2.47q^{-2} \\ \overset{q\to 0}{\to} & 3.00q^{-2}. \end{cases} \tag{A.3b}$$

In fact, this is the reason that the diffusion approximation works so well for point scatterers. It explains the difference between equations (A.1) and (A.2) and, moreover, suggests that the diffusion approximation should improve considerably after a simple addition of the two-scatterer contribution. The θ^{-1} fall-off in the wings of the cone follows rigorously from this contribution. A θ^{-1} behaviour was also found in [24], though under completely different assumptions.

The wings of the two-scatterer vector cone can be estimated in the same way. Using equation (4.8)

$$\gamma_{C(2)}\left[\theta \gg (k_0\bar{l}_0)^{-1}\right] = \frac{9}{4}(k_0\bar{l}_0)^{-1} s(\theta) \int \frac{\mathrm{d}^3\boldsymbol{y}}{4\pi} \frac{\cos \boldsymbol{b}\cdot\boldsymbol{y}}{y^2} \left[(\boldsymbol{e}_{\boldsymbol{k}}\cdot\boldsymbol{e}'_{\boldsymbol{k}'})^2 + (\boldsymbol{e}_{\boldsymbol{k}}\cdot\hat{\boldsymbol{y}})^2(\boldsymbol{e}'_{\boldsymbol{k}'}\cdot\hat{\boldsymbol{y}})^2 - 2(\boldsymbol{e}_{\boldsymbol{k}}\cdot\boldsymbol{e}'_{\boldsymbol{k}'})(\boldsymbol{e}_{\boldsymbol{k}}\cdot\hat{\boldsymbol{y}})(\boldsymbol{e}'_{\boldsymbol{k}'}\cdot\hat{\boldsymbol{y}})\right].$$

The angular integral is

$$(\boldsymbol{e}_{\boldsymbol{k}}\cdot\boldsymbol{e}'_{\boldsymbol{k}'})^2 j_0(by) + \left[1 + 2(\boldsymbol{e}_{\boldsymbol{k}}\cdot\boldsymbol{e}'_{\boldsymbol{k}'})^2\right]\frac{j_2(by)}{(by)^2} + \left(\boldsymbol{e}_{\boldsymbol{k}}\cdot\hat{\boldsymbol{b}}\right)^2\left(\boldsymbol{e}'_{\boldsymbol{k}'}\cdot\hat{\boldsymbol{b}}\right)^2 j_4(by)$$
$$- \left[\left(\hat{\boldsymbol{b}}\cdot\boldsymbol{e}_{\boldsymbol{k}}\right)^2 + \left(\hat{\boldsymbol{b}}\cdot\boldsymbol{e}'_{\boldsymbol{k}'}\right)^2 + 4(\boldsymbol{e}_{\boldsymbol{k}}\cdot\boldsymbol{e}'_{\boldsymbol{k}'})\left(\boldsymbol{e}_{\boldsymbol{k}}\cdot\hat{\boldsymbol{b}}\right)\left(\boldsymbol{e}'_{\boldsymbol{k}'}\cdot\hat{\boldsymbol{b}}\right)\right]\frac{j_3(by)}{by}$$
$$- 2(\boldsymbol{e}_{\boldsymbol{k}}\cdot\boldsymbol{e}'_{\boldsymbol{k}'})^2\frac{j_1(by)}{by} + 2(\boldsymbol{e}_{\boldsymbol{k}}\cdot\boldsymbol{e}'_{\boldsymbol{k}'})\left(\boldsymbol{e}_{\boldsymbol{k}}\cdot\hat{\boldsymbol{b}}\right)\left(\boldsymbol{e}'_{\boldsymbol{k}'}\cdot\hat{\boldsymbol{b}}\right) j_2(by)$$

where j_m is the spherical Bessel function of the first kind of order m, and $\hat{\boldsymbol{b}} \equiv \boldsymbol{b}/b$. Using the standard integral [23]

$$\int_0^\infty \mathrm{d}x \, \frac{j_n(x)}{x^m} = \frac{\pi^{1/2}}{2} 2^{-m} \frac{\Gamma\left(\frac{1}{2} + \frac{1}{2}(n-m)\right)}{\Gamma\left(1 + \frac{1}{2}(n+m)\right)}$$

the wings can be shown to be equal to

$$\gamma_{C(2)}[\theta \gg (k_0 \bar{l}_0)^{-1}] = \tfrac{9}{4} \left(k_0 \bar{l}_0\right)^{-1} s(\theta) \frac{\pi}{b} \mathcal{W}(\boldsymbol{e}_{\boldsymbol{k}}, \boldsymbol{e}'_{\boldsymbol{k}'}, \hat{\boldsymbol{b}}) \tag{A.4}$$

where

$$\begin{aligned} \mathcal{W}(\boldsymbol{e}_{\boldsymbol{k}}, \boldsymbol{e}'_{\boldsymbol{k}'}, \hat{\boldsymbol{b}}) = {} & \tfrac{1}{8}(\boldsymbol{e}_{\boldsymbol{k}} \cdot \boldsymbol{e}'_{\boldsymbol{k}'})^2 + \tfrac{1}{16} + \tfrac{3}{16}(\hat{\boldsymbol{b}} \cdot \boldsymbol{e}_{\boldsymbol{k}})^2 (\hat{\boldsymbol{b}} \cdot \boldsymbol{e}'_{\boldsymbol{k}'})^2 \\ & - \tfrac{1}{16}[(\hat{\boldsymbol{b}} \cdot \boldsymbol{e}_{\boldsymbol{k}})^2 + (\hat{\boldsymbol{b}} \cdot \boldsymbol{e}'_{\boldsymbol{k}'})^2] + \tfrac{1}{4}(\boldsymbol{e}_{\boldsymbol{k}} \cdot \boldsymbol{e}'_{\boldsymbol{k}'})(\hat{\boldsymbol{b}} \cdot \boldsymbol{e}_{\boldsymbol{k}})(\hat{\boldsymbol{b}} \cdot \boldsymbol{e}'_{\boldsymbol{k}'}). \end{aligned}$$

The complex nature of the function $\mathcal{W}$ clearly illustrates the anisotropy of the vector cone. The vector $\hat{\boldsymbol{b}}$ is given by $\hat{\boldsymbol{b}} = \sin\frac{1}{2}\theta \hat{\boldsymbol{z}} + \cos\frac{1}{2}\theta \hat{\boldsymbol{R}}$ where $\hat{\boldsymbol{z}}$ is perpendicular to the slab, and $\hat{\boldsymbol{R}}$ parallel. We set $\hat{\boldsymbol{R}} = \cos\phi \hat{\boldsymbol{x}} + \sin\phi \hat{\boldsymbol{y}}$ and define the direction of the incoming polarisation $\boldsymbol{e}_{\boldsymbol{k}} = \hat{\boldsymbol{y}}$. To calculate the anisotropy of the wings, we distinguish [7] two cases: case I has $\phi = 0, \pi$, and case II has $\phi = -\pi/2, \pi/2$. Let us assume $\theta \equiv \mu/k_0\bar{l}_0 \ll 1$. Then $\hat{\boldsymbol{b}} = \hat{\boldsymbol{R}}$ and it follows for the wings in the co-polarised channel ($\boldsymbol{e}_{\boldsymbol{k}} \parallel \boldsymbol{e}'_{\boldsymbol{k}'}$) that

$$\begin{aligned} &\gamma_{C(2)}(\text{co-pol}) = \tfrac{9}{128}\pi(3 + 5\sin^2\phi)\mu^{-1} \\ &\gamma_{C(2)}(\text{co-pol, I}) = 0.66\mu^{-1} \\ &\gamma_{C(2)}(\text{co-pol, II}) = 1.77\mu^{-1}. \end{aligned} \tag{A.5}$$

The co-polarised two-scatterer wing for case I compares well with the scalar result in equation (A.1). Both for the scalar case and the co-polarised Rayleigh case we find the μ^{-1} fall-off. For the cross-polarised channel ($\boldsymbol{e}_{\boldsymbol{k}} \perp \boldsymbol{e}'_{\boldsymbol{k}'}$) we find that

$$\gamma_{C(2)}(\text{cross}) = \tfrac{27}{512}\pi \sin^2 2\phi \, \mu^{-1}. \tag{A.6}$$

We see that, for the cases I and II, equation (A.6) vanishes, and we need higher orders in $(k\bar{l})^{-1}$. By expanding the extinction factors in the bistatic coefficient of the cone it follows, after some manipulations, that

$$\gamma_{C(2)}(\text{cross, I and II}) = \tfrac{21}{64}\mu^{-2} = 0.33\mu^{-2}. \tag{A.7}$$

From equation (A.5) we infer that the wings of case II in the co-polarised channel are, in case of point scatterers, more pronounced than for case I, in agreement with [7]. More precisely I : II = 3 : 8. The cross-polarised wings are the same for both case I and II, and are narrower. For fixed θ they reach a maximum at $\phi = \pi/4, -\pi/4$, thus exactly in between the directions of both polarisation vectors. In that case

$$\frac{\gamma_{C(2)}(\text{co-pol})}{\gamma_{C(2)}(\text{cross})} = \frac{22}{3} \tag{A.8}$$

independent of θ.

A μ^{-2} fall-off was also found by Stephen and Cwilich [4] on the basis of the diffusion approximation, though for *both* channels. As is demonstrated in equation (A.3*a*) for scalar waves, this is essentially due to neglect of the two-scatterer contribution. The exact wings in the cross-polarised channel are estimated by the sum of the diffusive part found by Stephen and Cwilich and the two-scatterer contribution equations (A.6) and (A.7).

It was shown numerically by van Albada and Lagendijk [6] that for long light paths, anisotropic effects can be completely neglected. Consequently, any theory incorporating the diffusion approximation will not be able to account for spatial anisotropy in the backscattered signal of vector waves. The wings of the cone are, by Fourier transformation, determined by short light paths. Therefore, the exact quantitative results equations (A.5)–(A.8) are subject to direct experimental verification.

Equation (A.4) is easily generalised for the case of circularly polarised light. Then the polarisation vectors become complex-valued. If the incoming and outgoing waves have the same helicities, we set, at backscattering where $\boldsymbol{k}' = -\boldsymbol{k}$

$$\boldsymbol{e}_{\boldsymbol{k}} = \boldsymbol{e}'^{*}_{\boldsymbol{k}'} = \tfrac{1}{2}2^{1/2}(\hat{\boldsymbol{x}} + \mathrm{i}\hat{\boldsymbol{y}}) \tag{A.9a}$$

and for opposite helicity

$$\boldsymbol{e}_{\boldsymbol{k}} = \boldsymbol{e}'_{\boldsymbol{k}'} = \tfrac{1}{2}2^{1/2}(\hat{\boldsymbol{x}} + \mathrm{i}\hat{\boldsymbol{y}}). \tag{A.9b}$$

It follows that

$$|\boldsymbol{e}_{\boldsymbol{k}} \cdot \hat{\boldsymbol{b}}|^2 = |\boldsymbol{e}'_{\boldsymbol{k}'} \cdot \hat{\boldsymbol{b}}|^2 = \tfrac{1}{2}$$

independent of ϕ. Using the complex equivalent of equation (A.4) we calculate for the wings in the opposite helicity channel

$$\gamma_{C(2)}(\text{opp.}) = \tfrac{171}{512}\pi\mu^{-1} = 1.05\mu^{-1} \tag{A.10a}$$

and in the helicity-preserving channel

$$\gamma_{C(2)}(\text{pres.}) = \tfrac{27}{512}\pi\mu^{-1} = 0.17\mu^{-1}. \tag{A.10b}$$

Both helicity channels exhibit the θ^{-1} fall-off, and are *independent* of ϕ. The absence of anisotropic effects makes the wings very similar to the scalar wings in equation (A.1). The similarity in the enhanced backscattering of scalar waves and vector waves in the helicity-preserving channel was noticed by MacKintosh and John [5], on the basis of the diffusion approximation.

We emphasise that this analysis is valid for point scatterers with a Rayleigh phase function. For Mie scatterers with 'hard sphere radius' a, equations (A.5), (A.6) and (A.10) are expected to apply in the regime

$$(k\bar{l})^{-1} < \theta < 1 < (ka)^{-1} \tag{A.11}$$

provided it exists. A backscattering angle larger than $1/ka$ probes a light path shorter than the 'size' of the scatterers. This regime is expected to be strongly influenced by pair correlation. The phase function of a Mie scatterer is in Rayleigh form if $ka < 1$. In that case the right hand side in equation (A.11) is satisfied.

Appendix B High-order loops for scalar waves

The total incoherent ladder sum for scalar isotropic point scatterers is characterised by a diffusion propagator $F(\boldsymbol{x}_1, \boldsymbol{x}_2)$ that satisfies the integral equation [2]

$$F(\boldsymbol{x}_1, \boldsymbol{x}_2) = n^2 |t|^4 |G^2(\boldsymbol{x}_{12})| + n|t|^2 \int_{\text{slab}} \mathrm{d}^3\boldsymbol{x}_0 \, |G^2(\boldsymbol{x}_1, \boldsymbol{x}_0)| F(\boldsymbol{x}_0, \boldsymbol{x}_2). \tag{B.1}$$

In the backward direction, the contribution of the loops involving three scattering events or more (figure 6) to the bistatic coefficient is given by

$$\begin{aligned}\gamma = \left(\frac{A}{4\pi}\right)^{-1} 2\frac{n|t|^4}{(4\pi)^2} \int \cdots \int \mathrm{d}^3\boldsymbol{x}_0 \, \mathrm{d}^3\boldsymbol{x}_1 \, \mathrm{d}^3\boldsymbol{x}_2 \, \mathrm{d}^3\boldsymbol{x}_3 \, \mathrm{d}^3\boldsymbol{x}_4 \, G(\boldsymbol{x}_{01}) G^*(\boldsymbol{x}_{02}) F(\boldsymbol{x}_1, \boldsymbol{x}_3) \\ \times \delta(\boldsymbol{x}_1 - \boldsymbol{x}_2) \delta(\boldsymbol{x}_3 - \boldsymbol{x}_4) G(\boldsymbol{x}_{03}) G^*(\boldsymbol{x}_{04}) \exp(-2z_0/\bar{l}_0) \\ = \left(\frac{A}{4\pi}\right)^{-1} 2\frac{n|t|^4}{(4\pi)^2} \iiint \mathrm{d}^3\boldsymbol{x}_0 \, \mathrm{d}^3\boldsymbol{x}_1 \, \mathrm{d}^3\boldsymbol{x}_3 \\ \times |G(\boldsymbol{x}_{01})|^2 F(\boldsymbol{x}_1, \boldsymbol{x}_3) |G(\boldsymbol{x}_{03})|^2 \exp(-2\tau_0).\end{aligned}$$

An extra factor of two comes in because the loops with inner most-crossed diagrams equal the loops with inner ladders. Defining

$$\begin{aligned} D(\boldsymbol{x}_1, \boldsymbol{x}_2) &\equiv \bar{l}_0^2 F(\boldsymbol{x}_1, \boldsymbol{x}_2) \\ A(\boldsymbol{x}_{12}) &\equiv (4\pi)^2 |G^2(\boldsymbol{x}_{12})| \end{aligned}$$

equation (B.1) becomes, using the optical theorem equation (2.3*a*)

$$D(\boldsymbol{x}_1, \boldsymbol{x}_2) = A(\boldsymbol{x}_{12}) + (4\pi\bar{l}_0)^{-1} \int_{\text{slab}} \mathrm{d}^3\boldsymbol{x}_0 \, A(\boldsymbol{x}_{10}) D(\boldsymbol{x}_0, \boldsymbol{x}_2). \tag{B.2}$$

Various orders can be identified using

$$D^{(j+1)}(\boldsymbol{x}_1, \boldsymbol{x}_2) = (4\pi\bar{l}_0)^{-1} \int_{\text{slab}} \mathrm{d}^3\boldsymbol{x}_0 \, A(\boldsymbol{x}_{10}) D^{(j)}(\boldsymbol{x}_0, \boldsymbol{x}_2) \tag{B.3}$$

and $D^{(1)} \equiv D$. It follows, using equation (B.3), that

$$\gamma = 2\frac{|\tilde{t}^2|}{(k_0\bar{l}_0)^2} \int_0^\tau \mathrm{d}\tau_0 \, D^{(3)}(\tau_0, \tau_0) \exp(-2\tau_0). \tag{B.4}$$

We have set $\tilde{t} \equiv (4\pi/k)^{-1} t$; τ is the optical depth of the slab. It is readily seen in reciprocal space, using the translationally invariant expression for D that both $D^{(2)}(0)$ and $D^{(3)}(0)$ are infinite, that is: low-order loops suffer from an UV singularity. In fact, the singularity of $D^{(3)}$ is logarithmic. For $n \geq 4$ the loops sum to

$$\gamma(n \geq 4) = 2\frac{|\tilde{t}^2|}{(k_0\bar{l}_0)^2} \int_0^\tau \mathrm{d}\tau_0 \, D^{(4)}(\tau_0, \tau_0) \exp(-2\tau_0). \tag{B.5}$$

The kernel D is translationally invariant *along* the slab but not perpendicular to it. To account for this we use the method of images [2, 5]: for any optical depth the diffusion propagator is assumed to be given by

$$D\left(\tau_1, \tau_2, \boldsymbol{x}_{12\|}\right) = \sum_{m=-\infty}^{\infty} D_{\mathrm{TS}}\left(\tau_1 - \tau_2 + m\beta, \boldsymbol{x}_{12\|}\right) - D_{\mathrm{TS}}\left(\tau_1 + \tau_2 + m\beta + 2z_0, \boldsymbol{x}_{12\|}\right) \tag{B.6}$$

where $\beta = 2(\tau + 2z_0)$ and $z_0 = 0.7104$; D_{TS} is the translationally symmetric diffusion propagator. The method of images becomes exact in the diffusion limit which incorporates long light paths only. In fact the long light paths (in this case long loops) suffer most from the finiteness of the slab and we assume equation (B.6) to hold rigorously. Substitution of equation (B.6) and applying Poisson's summation rule

$$\frac{1}{2\pi} \sum_{m=-\infty}^{\infty} \exp(imx) = \sum_{j=-\infty}^{\infty} \delta(x - 2\pi j) \tag{B.7}$$

equation (B.5) can be written as

$$\gamma(n \geq 4) = 4 \frac{|\tilde{t}^2|}{(k_0 \bar{l}_0)^2} \frac{1}{\beta} \sum_{j=-\infty}^{\infty} K_{\mathrm{B}}(\tau, q_j) \int \frac{\mathrm{d}^2 \boldsymbol{q}}{4\pi} \mathcal{F}(\boldsymbol{q}, q_j) \tag{B.8}$$

where

$$K_{\mathrm{B}}(\tau, q) = 1 - \exp(-2\tau) - \frac{[1 - \exp(-2\tau)\exp(2\mathrm{i}\tau q)]\exp(2\mathrm{i}z_0 q)}{1 - \mathrm{i}q}.$$

We have set $q_j = (2\pi/\beta)j$ and

$$\mathcal{F}(\boldsymbol{q}) = \frac{(\tan^{-1} q/q)^4}{1 - \tan^{-1} q/q}.$$

For a semi-infinite slab this reduces to an integral

$$\lim_{\tau \to \infty} \gamma(n \geq 4) = \frac{|\tilde{t}^2|}{(k_0 \bar{l}_0)^2} \frac{4}{2\pi} \int \frac{\mathrm{d}^3 \boldsymbol{q}}{4\pi} \mathcal{F}(q) \left(1 - \frac{\exp(2\mathrm{i}z_0 q_z)}{1 - \mathrm{i}q_z}\right) = 2.6028 \frac{|\tilde{t}^2|}{(k_0 \bar{l}_0)^2}. \tag{B.9}$$

In the forward direction the same formula (B.8) applies, but now

$$K_{\mathrm{F}}(\tau, q) = 2\tau \exp(-\tau)\left(1 - \exp(\mathrm{i}\beta q)\frac{\sin \tau q}{\tau q}\right). \tag{B.10}$$

Neglecting the second term between straight brackets is actually the infinite space approximation, and is good for large q, e.g. short loops.

For the three-scatterer loops the calculation is analogous. In the backward direction for a semi-infinite slab

$$\gamma_{\mathcal{L}(3)} = \frac{4}{2\pi} \frac{|\tilde{t}|^2}{(k_0 \bar{l}_0)^2} \int \frac{\mathrm{d}^3 \boldsymbol{q}}{4\pi} \tilde{A}^3(q) \left(1 - \frac{\exp(2\mathrm{i}q_z z_0)}{1 - \mathrm{i}q_z}\right). \tag{B.11}$$

Here $\tilde{A}(q)$ is the UV-renormalised variant of $A(q) \equiv \tan^{-1} q/q$, and is found by Fourier transformation

$$\tilde{A}(q) \equiv \int \mathrm{d}^3\boldsymbol{x}\, \frac{|G^2(x)|}{|1-t^2G^2(x)|^2} \exp(\mathrm{i}\boldsymbol{q}\cdot\boldsymbol{x}). \tag{B.12}$$

This renormalisation provides an upper cut-off in equation (B.11): $q_c \approx k_0\bar{l}_0/|\tilde{t}|$.

The method of images cannot be used to calculate the forward cone for all angles, and we must rely on the infinite space approximation. If we neglect angle dependence as result of extinction we obtain for the bistatic coefficient of the cone involving four scatterers and more

$$\begin{aligned}\gamma_{\mathcal{F}(n\geq 4)}(\theta) \approx \left(\frac{A}{4\pi}\right)^{-1} 2\frac{n^2|t|^6}{(4\pi)^2}\exp(-\tau) \\ \times \int_{\mathrm{slab}} \mathrm{d}^3\boldsymbol{x}_0 \int_{\mathrm{R}^3} \mathrm{d}^3\boldsymbol{x}_{10} \int_{\mathrm{R}^3} \mathrm{d}^3\boldsymbol{x}_{20} |G^2(\boldsymbol{x}_{01})| F_{\mathrm{TS}}^{(2)}(\boldsymbol{x}_{12})| G^2(\boldsymbol{x}_{20})| \\ \times \exp(\mathrm{i}\boldsymbol{f}\cdot\boldsymbol{x}_{10})\end{aligned} \tag{B.13}$$

with $\boldsymbol{f} \equiv \boldsymbol{k} - \boldsymbol{k}'$. This simplifies to equation (5.3) using the convolution theorem. The first integral is set equal to $A\bar{l}_0\tau$.

Next, let us consider the forward cone resulting from the interference of two loops involving three scatterers. We show that this scattering event does *not* yield a narrow cone. Again we rely on the 'infinite space approximation' and assume that the renormalisation procedure in equation (B.12) can simply be replaced by the cut-off in reciprocal space: $q_c \approx k_0\bar{l}_0/|\tilde{t}|$. It then follows, as in equation (5.3), that

$$\gamma_{\mathcal{F}(3)}(\theta) \approx \frac{4}{\pi}\frac{|\tilde{t}|^2}{(k_0\bar{l}_0)^2}\tau\exp(-\tau)C_3(f)$$

with

$$C_3(f) = \int_{q\leq q_c} \frac{\mathrm{d}^3\boldsymbol{q}}{4\pi} A^2(q)A(\boldsymbol{q}+\boldsymbol{f}) \tag{B.14}$$

where now $\boldsymbol{f} \equiv \bar{l}_0(\boldsymbol{k}-\mathbf{k}')$. In the wings we have $f > 1$ and we approximate $A(\boldsymbol{q}+\boldsymbol{f}) \approx (\pi/2)|\boldsymbol{q}+\boldsymbol{f}|^{-1}$. Performing the angular integration gives

$$C_3(f) \approx \frac{\pi}{2}\int_0^{q_c} \mathrm{d}q\, \frac{(\tan^{-1})^2 q}{\max(f,q)} \approx \frac{\pi}{2}f^{-1}\int_0^f \mathrm{d}q\,(\tan^{-1}q)^2 + \left(\frac{\pi}{2}\right)^3 \log\frac{q_c}{f}. \tag{B.15}$$

This rough estimate shows that the angle dependence is logarithmic and thus very broad.

Appendix C Longitudinal corrections to the vector Green function

This appendix deals with the asymptotic behaviour of the second term in equation (3.11) for the amplitude Green function for Rayleigh point scatterers

$$\Delta\boldsymbol{G}(\boldsymbol{x}) = \frac{1}{z^2}\int \frac{\mathrm{d}^3\boldsymbol{p}}{(2\pi)^3}\frac{\Sigma_a(p)}{z^2-\Sigma_a(p)}\hat{\boldsymbol{p}}\hat{\boldsymbol{p}}\exp(\mathrm{i}\boldsymbol{p}\cdot\boldsymbol{x}) \tag{C.1}$$

where we have set the isotropic self-energy on the shell ($p = k_0$). This simplification defines the complex wavenumber $z^2 \equiv k_0^2 - \Sigma_i(k_0)$ and guarantees exponential decay of the part of the Green function given by the first term of equation (3.11). Following our self-consistent scheme of section 3 the transverse wave P and the longitudinal wave Q appearing in the equations of the self-energy equation (3.9) should be renormalised as well. This makes it possible to continue the expression for $\Sigma_a(p)$ analytically into the sheet

$$0 < \mathrm{Im}\, p < 3\,\mathrm{Im}\, z.$$

Let us ignore the possible locations of singularities in this sheet coming from the denominator of the integrand in equation (C.1) and assume that it is essentially p-independent: $z^2 - \Sigma_a(p) \approx z^2$. As is shown in section 3 this is a very good approximation. Then the above proves that equation (C.1) is exponentially damped with a decay length which is at least smaller than $\bar{l}/3$. To investigate the behaviour for large x we use the expression for $\Sigma_a(p)$ equation (3.9)

$$\begin{aligned}\Delta \boldsymbol{G}(\boldsymbol{x}) &= -\frac{1}{z^4}\frac{\partial}{\partial \boldsymbol{x}}\frac{\partial}{\partial \boldsymbol{x}}\int \frac{\mathrm{d}^3\boldsymbol{p}}{(2\pi)^3}\frac{\Sigma_a(p)}{p^2}\exp(\mathrm{i}\boldsymbol{p}\cdot\boldsymbol{x}) \\ &= -\frac{n^2t^4}{2\pi^2 z^4}\frac{\partial}{\partial \boldsymbol{x}}\frac{\partial}{\partial \boldsymbol{x}}\int_0^\infty \mathrm{d}y\, F(y)\int_0^\infty \mathrm{d}p\, j_0(px)j_2(py)\end{aligned}$$

where we have defined

$$F(y) \equiv y^2\left(\frac{P^3}{1-t^2P^2} - \frac{Q^3}{1-t^2Q^2}\right). \tag{C.2}$$

Here $P = P(zy), Q = Q(zy)$ defined in equation (2.2d). The integral with the two spherical Bessel functions is [23]

$$\int_0^\infty \mathrm{d}p\, j_0(px)j_2(py) = \frac{\pi}{4}\frac{y^2-x^2}{y^3}\Theta(y-x). \tag{C.3}$$

Hence

$$\Delta \boldsymbol{G}(\boldsymbol{x}) = -\frac{n^2t^4}{8\pi z^4}\frac{\partial}{\partial \boldsymbol{x}}\frac{\partial}{\partial \boldsymbol{x}}\int_1^\infty \mathrm{d}s\, F(sx)\frac{s^2-1}{s^3}. \tag{C.4}$$

By an asymptotical analysis we can infer

$$\Delta \boldsymbol{G}(\boldsymbol{x}) \overset{x\to\infty}{\to} -\frac{n^2t^4}{z^4}\frac{\exp(3\mathrm{i}zx)}{4\pi x^3}\hat{\boldsymbol{x}}\hat{\boldsymbol{x}}. \tag{C.5}$$

This expression proves that we are dealing with a strongly damped longitudinal mode with decay length $\bar{l}/3$. For weak disorder, this mode is therefore not of any importance. For large packing fractions it can, however, become important. If the Green functions in the expression of $\Sigma_a(p)$ are not renormalised, then $\Sigma_a(p)$ cannot be analytically continued in a strip along the real axis. Consequently, $\Delta \boldsymbol{G}(\boldsymbol{x})$ would not be exponentially damped. Care should therefore be taken with density expansions in the self-energy.

References

[1] van de Hulst H C 1980 *Multiple Light Scattering* vol 1 (New York: Academic)
[2] van der Mark M B, van Albada M P and Lagendijk A 1988 *Phys. Rev.* B **37** 3575
[3] Akkermans E, Wolf P E and Maynard R 1986 *Phys. Rev. Lett.* **56** 1471
[4] Stephen M J and Cwilich G 1986 *Phys. Rev.* B **34** 7564
[5] MacKintosh F C and John S 1988 *Phys. Rev.* B **37** 1885
[6] van Albada M P and Lagendijk A 1987 *Phys. Rev.* **36** 2353
[7] van Albada M B, van der Mark M B and Lagendijk A 1988 *J. Phys. D: Appl. Phys.* **21** S28
[8] Vollhardt D and Wölfe P 1980 *Phys. Rev.* B **22** 4666
[9] Kirkpatrick T R 1985 *Phys. Rev.* B **31** 5746
[10] Souillard B 1986 *Chance and Matter (Les Houches. 1986)* session 46, ed J Souletie, J Vannimenus and R Stora (Amsterdam: North-Holland)
[11] Albeverio S, Gesztesy F, Høegh-Krohn R and Holden H 1988 *Solvable Models in Quantum Mechanics* (New York: Springer)
[12] Grossmann A and Wu T T 1984 *J. Math. Phys.* **25** 1742
[13] Wu T T 1984 *Resonances — Models and Phenomena* ed S Albeverio, L S Ferreira and L Streit (Berlin: Springer)
[14] van Diejen J F and Tip A 1990 submitted
[15] Peterson B and Ström S 1973 *Phys. Rev.* D **10** 3661
[16] van der Hulst H C 1981 *Light Scattering by Small Particles* (New York: Dover)
[17] Waterman P C 1971 *Phys. Rev.* D **3** 825
[18] Bringi V N, Seliga T A, Varadan V K and Varadan V V 1980 *Multiple Scattering and Waves in Random Media* ed P L Chow, W E Kohler and G C Papanicolaou (Amsterdam: North-Holland)
[19] Frisch U 1968 *Probabilistic Methods in Applied Mathematics* vol 1, ed A T Barucha-Reid (New York: Academic)
[20] Reiter G F and Lagendijk A 1988 unpublished
[21] Ishimaru A 1978 *Wave Propagation in Random Media* vols 1 and 2 (New York: Academic)
[22] Mahan G D 1981 *Many Particle Physics* (New York: Plenum)
[23] Gradshteyn R 1980 *Table of Integrals, Series and Products* (New York: Academic)
[24] Schmeltzer D and Kaveh M 1987 *J. Phys. C: Solid State Phys.* **20** L175